# 論文 / 著書情報
# Article / Book Information

| | |
|---|---|
| Title | Slab surface passivation and its application to band offset calculations for polar heterointerfaces of zinc-blende semiconductors |
| Authors | Tianwei Wang, Fumiyasu Oba |
| Citation | Physical Review Materials, vol. 7, Issue 8, pp. 084602-1-12 |
| Pub. date | 2023, 8 |
| Copyright | (c) 2023 American Physical Society |
| DOI | https://dx.doi.org/10.1103/PhysRevMaterials.7.084602 |

# Slab surface passivation and its application to band offset calculations for polar heterointerfaces of zinc-blende semiconductors

Tianwei Wang * and Fumiyasu Oba †

*Laboratory for Materials and Structures, Institute of Innovative Research, Tokyo Institute of Technology, Yokohama 226-8503, Japan*

(Received 8 March 2023; accepted 7 July 2023; published 8 August 2023)

The band offsets at polar heterointerfaces that consist of group III-V zinc-blende semiconductors are investigated by first-principles modeling using the Heyd-Scuseria-Ernzerhof hybrid functional. Since the band alignment for such polar heterointerfaces and their constituent polar surfaces has not been fully elucidated and a reliable computational setup remains lacking, we propose in this paper the application of pseudo-H passivation in combination with the supercell approach adopting slab models. The pseudo-H passivation is shown to be a valid computational setup that quenches the macroscopic electric field generated by polar slab surfaces and stabilizes the electrostatic potential profile normal to the surfaces, and more consequentially, across the polar interface in the slab. This is essential to an accurate evaluation of the band offset at a polar interface using the supercell approach. The interfaces made of the polar (100) or (111) surfaces of AlP, AlAs, GaP, GaAs, InP, and InAs are studied. The predicted valence-band offsets are in good agreement with available experimental results. The offset values of most interfaces show weak dependence on their local chemical compositions, which is attributed to the formation of nearly complete interfacial chemical bonding.

DOI: 10.1103/PhysRevMaterials.7.084602

## I. INTRODUCTION

The design of state-of-art electronic devices enormously depends on the band positions of the constituent semiconductors/insulators forming interfaces or surfaces [1–3] as well as their band alignment with other device components [4,5], such as metallic electrodes. In particular, the surface band alignment is rather dependent on the surface dipole controlled by the surface structure and composition [6–8]. The interfacial geometry and chemistry are also critical to determining the band offsets at heterojunctions [2–4,8,9]. Therefore, a better understanding of the dipole contribution to device interfaces and surfaces should be achieved to fully control and design their relative band positions.

A variety of computational setups adopting first-principles calculations have been proposed to predict the band offsets at different heterojunctions. Examples of such setups are the approximation made using the branch-point energies of the band structures obtained in bulk calculations [4,10–12], the approximation made according to point-defect transition levels [13–15], the representation obtained using the band edges at the surfaces of interest, i.e., the valence-band maximum (VBM) and the conduction-band minimum (CBM) with respect to the vacuum level [16–20], and the direct modeling of a certain heterointerface [8,9,21–23].

The energy difference between the vacuum level and the VBM is referred to as the ionization potential (IP) and that between the vacuum level and the CBM is the electron affinity (EA). These quantities serve as reasonable estimations of the band offsets at heterojunctions when the change in interfacial dipole contribution is insignificant compared with those at separated surfaces [8,9]. A representative example of this is a certain heterointerface that consists of nonpolar surfaces of isostructural materials with similar lattice parameters and chemical compositions [9,23], in which the interfacial dipole is well quenched by the negligible discontinuity in the atomic arrangement and the chemical bonding across the interface.

When the impact of the interfacial dipole is large, the direct modeling of the interface becomes indispensable [1,4]. However, the dislocations due to lattice mismatches and the incoherent atomic geometries commonly observed for heterojunctions significantly increase the complexity of modeling such interfaces using atomistic simulations including first-principles calculations, in which complex interface structures are either not transferable to the supercell approach under three-dimensional periodic boundary conditions (PBCs) or too refractory as a huge supercell size can hardly be avoided [24–26]. In contrast, modeling the interfaces with coherent atomic geometries is a convenient and efficient computational setup to study interfacial band offsets, in which similar lattice structures are matched and fitted into the same in-plane lattice parameter (ILP). Such a setup is particularly effective for experimentally observed coherent interfaces, where an epitaxial thin film below its critical thickness is strained on a substrate to achieve a common ILP [27]. This is also known as the "strained" band offset, although further corrections are needed to extract the "natural" band offsets that represent more commonly seen semicoherent and incoherent interfaces where the constituent crystals take their natural (unstrained) ILPs. These corrections usually involve the deformation potentials [22,28–30] or surface calculations to take into consideration the differences in EA and IP between an unstrained crystal

*wang@msl.titech.ac.jp
†oba@msl.titech.ac.jp

 

and that strained to a different ILP [8,9,17]. These works have provided useful insights into band offset calculations, but little has been discussed on polar heterointerfaces or their significant interfacial dipole contributions. Wadehra *et al.* [31] and Steiner *et al.* [32], adopting the superlattice approach, have investigated the strained band offsets at selected polar interfaces with negligible ILP mismatches (0.1–0.2%). Nevertheless, little is known if the superlattice approach is applicable to more commonly seen natural band offsets at interfaces with relatively larger ILP mismatches. Therefore, a more generalized computational scheme to investigate both the interface with a significant dipole contribution and its constituent polar surfaces is needed to obtain the natural band offset.

The modeling of polar surfaces and interfaces with strong dipole contributions has been a long-standing technical difficulty for first-principles calculations. The major issue lies in the formation of charged surfaces that are usually poorly described using the slab models within the supercell approach. This is due to the conflict between the long-ranged electrostatic interaction and the relatively small supercell used under the PBC scheme [33–36]. In addition, a macroscopic electric field forms when using a stoichiometric slab model for a compound, where two polar surfaces deviate from the stoichiometry in opposite directions, resulting in positive or negative surface charges [36–39]. Various compensation mechanisms for the macroscopic electric field have been proposed, among which those applicable to slab surfaces can be summarized into two major categories. The first well-known mechanism uses ionic transfer, in which atoms from one surface of the slab are relocated to the other, forming adatoms and vacancies that partially cancel out the macroscopic electric field. This mechanism has been proven effective by various studies, especially on surface reconstruction and reactivity [35,40]. The counter dipole generated by relocating atoms cannot, however, ideally reduce the macroscopic electric field to zero except for special crystal and surface geometries; thus, applying a finite electric field to the supercell is usually necessary to remove the residual electric field [36,41]. This finite electric field together with the complexity in predicting the reconstructed surfaces with adatoms or vacancies has made this mechanism less transferable to the objective of calculating interfacial band offsets, as the computational setup can hardly hold from surface to interface calculations. A special case of the first mechanism ideally forms a nonpolar surface [19,42], which is usually categorized as one of Tasker's type-3 surfaces [43] but particularly follows the type-C arrangement defined by Hinuma *et al.* [39]. Therefore, such type-C facet geometries also depend on a successful prediction of the reconstructed surfaces. The second mechanism aims to prevent surface charge transfer through proper surface passivation so that the constructed slab amounts to a semi-infinite bulk system [44–46] that quenches the macroscopic electric field. Proper passivation and slab thickness help eliminate the impact of the passivated surface and allow for a more detailed study on the surface of interest (the free surface without passivation), such as the surface dangling bonds. A proper passivation treatment stabilizes the electrostatic potential along the thickness of the slab as well as that across the vacuum region from the perspective of first-principles calculations under the PBC scheme [46]. Thus, the passivation mechanism well fits our objective to investigate the band offsets at polar interfaces.

Since a well-established modeling method is still needed to evaluate the band offsets at polar interfaces and the impact of the interfacial dipole is not yet fully understood, we will present in this paper a computational scheme, utilizing slab surface passivation in combination with the first-principles technique, to investigate the band offsets at polar heterointerfaces. Band offset calculations for typical polar interfaces between group III-V zinc-blende (ZB) semiconductors, including AlP, AlAs, GaP, GaAs, InP, and InAs, are carried out to validate this computational scheme. In addition to the well-studied nonpolar (110) interfaces [8,22] and lattice-matched polar (100) interfaces [31,32], insights into more generalized polar (100) and (111) interfaces will be provided. Details of the passivation mechanism, the derivation of the natural band offset, and the first-principles calculations will be introduced in Sec. II, Computational Methods. The results and especially the validation of the passivation mechanism will then be given and discussed. This paper will be ended with a summary and an outlook for our future band offset calculations.

## II. COMPUTATIONAL METHODS

### A. Passivation using pseudo-H atoms

The ZB phase features a fourfold-coordinated interpenetrating structure of cations and anions so that the atomic planes in a polar orientation are composed of either only cations or anions, examples of which are the (100) and (111) atomic planes. Such an arrangement of the ions generates a macroscopic electric field that stacks up with each pair of cation and anion planes in a finite-sized system. Since the ZB phase has no further spontaneous polarization [47], the macroscopic dipole across the (100) atomic planes can be schematically illustrated in Fig. 1. As shown in Fig. 1(a), if a slab with a finite thickness and polar surfaces is not well passivated/stabilized, the electrostatic potential difference between the two surfaces will increase with slab thickness, forming the macroscopic electric field, and a dielectric breakdown will be expected when the slab thickness exceeds a critical value. Since the (100) surface of the ZB structure agrees with Hinuma's type-C definition [39], partial coverage is also a theoretically feasible alternative to eliminate the macroscopic electric field, as illustrated in Fig. 1(b). Figure 1(c) shows the desired passivation scenario to mimic a semi-infinite bulk system, in which the local surface dipoles still exist on the nonpassivated surface, but the macroscopic electric field will not stack up as the slab thickness increases, which is the key to dipole compensation. Both mechanisms in Figs. 1(b) and 1(c) help stabilize the electrostatic potential. Figure 1(d) further shows the application of the passivation mechanism to a polar interface model, in which the local interfacial dipole is preserved. In general, the passivation mechanism aims to eliminate the macroscopic electric field while maintaining the local interfacial or surface dipole contribution during the modeling of the electronic structure.

To better explain the passivation mechanism in Figs. 1(c) and 1(d), it is further resolved into the passivation of dangling

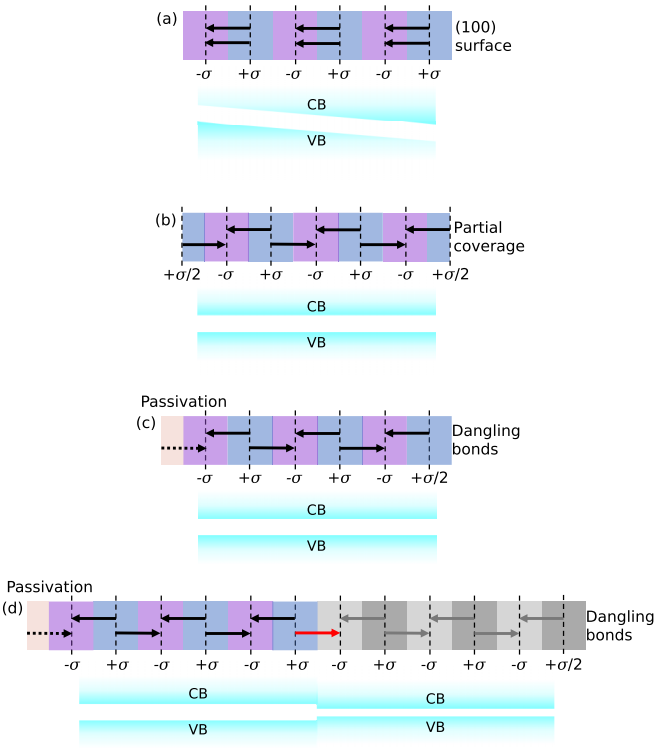


FIG. 1. Schematics of charge transfer and dipole contribution between six alternating (100) planes of a ZB structure. Four different mechanisms are provided: (a) nonpassivated polar surfaces, (b) stabilization using partial coverage, (c) the proposed surface passivation, and (d) the proposed passivation for an interfacial offset evaluation. Blue regions are cation planes, where each cation has a formal charge of $+\sigma$; purple regions are anion planes, where each anion has a formal charge of $-\sigma$; and pink regions represent the passivation. Dark- and light-gray regions in (d) are corresponding (100) $+\sigma$ cation and $-\sigma$ anion planes of another ZB semiconductor. Each pair of black arrows in (a) represents dipoles generated by counterions of $\pm\sigma$ at a distance of interplanar spacing. Regions indicated by $+\sigma/2$ in (b) denote that half of the cations are removed from original $+\sigma$ planes, whose dipole contribution is thus reduced by 50%, as indicated by one black arrow. Surface regions indicated by $+\sigma/2$ in (c) and (d) have full coverage but contribute to dipoles that are the same as half coverage because of the presence of partially occupied dangling bonds. Dashed arrows in (c) and (d) are compensating dipoles due to the passivation and indicate ideally the same dipole contribution as the solid arrows in black. The red arrow in (d) illustrates the local interfacial dipole and the gray arrows are dipoles in the second semiconductor that correspond to the black arrows in the first semiconductor. Corresponding profiles of valence bands (VB) and conduction bands (CB) of each case are schematically provided.

bonds following the electron-counting (EC) rule [48]. The passivation mechanism explained with the EC dangling bonds does not conflict with the uncompensated dipoles [46]. In other words, the local dipole due to passivation as denoted by the dashed arrow in Fig. 1(c) may not necessarily cancel out its counter local dipole, but the passivation is still valid since the macroscopic electric field does not stack up despite the presence of the local dipoles.

In the ZB crystal, each ion contributes to four identical bonds that form repeating tetrahedral structures. According to the EC rule, each of these four bonds is saturated by two electrons: $\sigma/4$ from the cation and $2-\sigma/4$ from the anion. Thus, the (100) surface terminated by twofold-coordinated anions (anion-t) can be passivated by a pair of pseudo-H (ps-H) atoms, each with a valence charge of $\sigma/4$ (also known as $H_{\sigma/4}$), and the twofold-coordinated cation-terminated (cation-t) surface can be passivated by a pair of $2-\sigma/4$ ps-H atoms ($H_{2-\sigma/4}$). These correspond with the illustration in Fig. 1(c). Similarly, the threefold-coordinated ions on the (111) surfaces can be passivated by one ps-H atom. The (111) surfaces terminated by onefold-coordinated ions are not considered in this work. This mechanism also applies to the dangling bonds on nonpolar surfaces. Schematics of these passivated surfaces are provided in Supplemental Material, Fig. S1 [49].

### B. Band alignments: IP, EA, and the natural interfacial band offset

IP is defined as the difference between the vacuum level and the VBM. The VBM offset at an interface can be approximated by the difference between the negative values of the IPs of the constituent phases, especially when the interfacial dipole contribution agrees well with the difference between the dipole contributions by the constituent surfaces. The IP can be derived by aligning the electrostatic potential of the surface model with its corresponding bulk model [20,50]. Since the absolute position of the reference level in an infinitely extending crystal is ill-defined [51], merely the difference between the VBM and the reference level can be obtained from the calculation of a bulk model as $\Delta\varepsilon_{\mathrm{VBM-Ref}}$. The absolute position of the reference level $\varepsilon_{\mathrm{Ref}}$ should be determined from a surface calculation on a slab of the same crystal, with respect to which the vacuum level can be calculated: $\Delta\varepsilon_{\mathrm{Vac-Ref}} = \varepsilon_{\mathrm{Vac}} - \varepsilon_{\mathrm{Ref}}$. Then, the IP is given by Eq. (1) that follows. Similarly, the EA can be obtained by Eq. (2) using the corresponding CBM:

$$\varepsilon_{\mathrm{IP}} = \Delta\varepsilon_{\mathrm{Vac-Ref}} - \Delta\varepsilon_{\mathrm{VBM-Ref}}, \tag{1}$$

$$\varepsilon_{\mathrm{EA}} = \Delta\varepsilon_{\mathrm{Vac-Ref}} - \Delta\varepsilon_{\mathrm{CBM-Ref}}. \tag{2}$$

In a practical surface calculation, the reference level $\varepsilon_{\mathrm{Ref}}$ was taken from the stabilized electrostatic potential of the bulklike region of the slab, whereas $\varepsilon_{\mathrm{Vac}}$ was taken from the stabilized electrostatic potential of the vacuum region. The stabilized electrostatic potential was determined by computing its planar average perpendicular to the slab thickness and the converged macroscopic average of the planar-averaged electrostatic potential was obtained for $\varepsilon_{\mathrm{Ref}}$ and $\varepsilon_{\mathrm{Vac}}$.

To derive the natural band offset at a heterointerface, the natural ILP difference between the constituent phases $A$ and $B$ needs to be considered. The interfacial dipole effect is typically estimated at a specific ILP $= X$ using a coherent interface model. $X$ thus denotes the ILP of the supercell that contains the interface. The contribution of the interfacial dipole is included by computing the difference between the reference levels of the interfaced phases $A$ and $B$, both biaxially strained to an interfacial ILP $= X$, and is denoted as $\Delta\varepsilon^{A-B}_{\mathrm{Ref},X}$. The contributions associated with the difference

between ILP $= X$ and ILP $= A$ or $B$ can be estimated using the deformation potentials [22,28–30] or band positions of surface models [8,9,17] with different ILPs. We take the latter approach in this study. Accordingly, the natural valence-band offset $\Delta\varepsilon_{\rm VBM}^{A-B,{\rm nat}}$ is given in Eq. (3). The uppercase $A$, $B$, or $X$ in the subscript of any term in Eq. (3) indicates the ILP used to calculate this very term:

$$\begin{aligned}&\Delta\varepsilon_{\rm VBM}^{A-B,{\rm nat}}\\&=\left(\Delta\varepsilon^{A}_{{\rm VBM-Ref},A}-\Delta\varepsilon^{A}_{{\rm Vac-Ref},A}+\Delta\varepsilon^{A}_{{\rm Vac-Ref},X}\right)\\&\quad+\Delta\varepsilon^{A-B}_{{\rm Ref},X}-\left(\Delta\varepsilon^{B}_{{\rm VBM-Ref},B}-\Delta\varepsilon^{B}_{{\rm Vac-Ref},B}+\Delta\varepsilon^{B}_{{\rm Vac-Ref},X}\right).\end{aligned}\tag{3}$$

The change in reference level with respect to the vacuum level due to varied ILPs is included by $-\Delta\varepsilon^{A}_{{\rm Vac-Ref},A}+\Delta\varepsilon^{A}_{{\rm Vac-Ref},X}$ and $-\Delta\varepsilon^{B}_{{\rm Vac-Ref},B}+\Delta\varepsilon^{B}_{{\rm Vac-Ref},X}$. Equation (3) thus requires calculations on four surfaces, one interface, and two bulk models. The choice of $X$ is arbitrary with respect to the ILPs of phases $A$ and $B$ [23]. Usually, $X$ takes the average of the ILPs of phases $A$ and $B$, and it can be denoted as $X=(A+B)/2$. However, to reduce the number of surface calculations, it is also reasonable to use $X=A$ or $X=B$ for small lattice-mismatch systems. The same setup is applicable to the CBM offset as shown in Eq. (4):

$$\begin{aligned}&\Delta\varepsilon_{\rm CBM}^{A-B,{\rm nat}}\\&=\left(\Delta\varepsilon^{A}_{{\rm CBM-Ref},A}-\Delta\varepsilon^{A}_{{\rm Vac-Ref},A}+\Delta\varepsilon^{A}_{{\rm Vac-Ref},X}\right)\\&\quad+\Delta\varepsilon^{A-B}_{{\rm Ref},X}-\left(\Delta\varepsilon^{B}_{{\rm CBM-Ref},B}-\Delta\varepsilon^{B}_{{\rm Vac-Ref},B}+\Delta\varepsilon^{B}_{{\rm Vac-Ref},X}\right).\end{aligned}\tag{4}$$

In this work, $X=A$ was mainly used and $X=(A+B)/2$ was considered for interfaces with an in-plane lattice mismatch of more than 1%.

### C. First-principles calculations

The calculations were performed using the projector augmented-wave (PAW) method [52] as implemented in the VASP code [53–56]. Under the generalized Kohn-Sham scheme [57,58], the exchange-correlation functional was approximated using the Heyd-Scuseria-Ernzerhof (HSE06) hybrid functional [59–61]. A plane-wave energy cutoff of 400 eV was chosen. The electronic structure calculations were carried out with a Gaussian smearing width of 0.05 eV. Gamma-centered $7\times7\times7$ $k$-point meshes were applied to the primitive cells of ZB semiconductors. A similar in-plane $k$-point density of 0.035 Å in each direction was used for all other associated surface and interface calculations. The atomic positions were optimized using the conjugate gradient method with a tolerance of 0.01 eV/Å for all force residuals. The PAW datasets included the valence states $3s$ and $3p$ with a radial cutoff of 1.0 Å for Al; $4s$, $4p$, $3d$, and 1.2 Å for Ga; $5s$, $5p$, $4d$, and 1.3 Å for In; $3s$, $3p$, and 1.0 Å for P; and $4s$, $4p$, and 1.1 Å for As.

The supercells for surface calculations were constructed using consecutive slabs separated by a vacuum region of 30 Å under the PBC scheme. Each slab contained 12 ZB (111) bilayers or 24 alternating (100) layers (both will be referred to as 12 bilayers in later sections) of $(1\times1)$ unit cells as shown in Fig. 2. The slab models were constructed using the

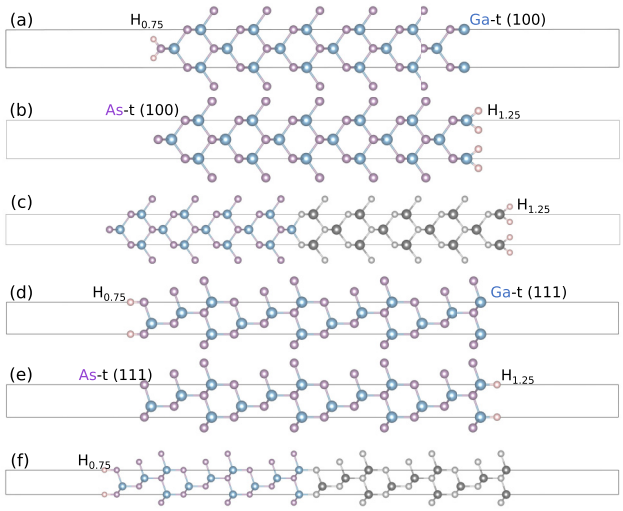


FIG. 2. Supercells for ZB (100) and (111) surface and interface calculations. As illustrated by GaAs, dangling bonds on the As-t surface are passivated by pairs of $H_{0.75}$ atoms in (a) for the free Ga-t (100) surface model and those on the Ga-t surface by pairs of $H_{1.25}$ in (b) for the free As-t (100) surface model. A polar (100) interface model is given in (c). The passivation of surface ions by a single ps-H atom is shown in (d) and (e) for the free (111) surface models. The setup for polar (111) interface calculations is given in (f). Spheres in blue are Ga atoms and those in purple are As atoms. Pink spheres represent the ps-H atoms. Spheres in gray stand for the second phase that forms an interface with GaAs.

HSE06-calculated lattice parameters. It can be seen in Table I that the HSE06 hybrid functional reasonably reproduces the lattice parameters and band gaps of the chosen ZB semiconductors. Thus, adopting these HSE06 lattice parameters in the following surface/interface calculations helped reduce artificial in-plane strains that might affect the band gaps and offsets. In addition, our previous study showed that HSE06 gave offset values close to the results of vertex-corrected $GW$ calculations on top of HSE06 for nonpolar (110) interfaces between group III-V ZB semiconductors ($\sim$0.1 eV or smaller differences for five types of interfaces) [8].

Only one side of the slab was passivated using the ps-H atoms as shown in Fig. 1(c). The charge of these ps-H atoms depended on the valence charge of the passivated ions. For example, $H_{0.75}$ atoms passivated the As-t (111) surface of GaAs, whereas the Ga-t surface was passivated by $H_{1.25}$ atoms. For a specific calculation of $\Delta\varepsilon^{B}_{{\rm Vac-Ref},X}$ with $X=B$, 6 (111) or (100) bilayers adjacent to the ps-H atoms were fixed and the other half of the slab was relaxed to optimize the surface atomic structures. The artificial electric field in the vacuum region was screened out by dipole correction [69]. When calculating $\Delta\varepsilon^{B}_{{\rm Vac-Ref},X}$ with $X\neq B$, phase $B$ was strained biaxially and only the outermost layer towards the ps-H atoms was fixed so that slab thickness was optimized with respect to a varied ILP. For simplicity, the cation termination is denoted by $A^{\rm cat}$ and the anion termination by $A^{\rm an}$, so that phases $A$ and $B$ form two opposite interfaces $A^{\rm cat}/B^{\rm an}$ and $A^{\rm an}/B^{\rm cat}$. Note that for (111) interfaces, only those consisting of surfaces terminated by threefold-coordinated ions are considered in

TABLE I. Theoretical lattice parameter $a$ (Å) and band gap $E_g$ (eV) values obtained using the HSE06 hybrid functional, in comparison with their corresponding experimental values. Effect of spin-orbit coupling (SOC) on each band gap is considered as reported in Ref. [18], in which the band gaps of AlP, GaP, InP, AlAs, GaAs, and InAs decrease by 0.02, 0.03, 0.00, 0.11, 0.12, and 0.12 eV, respectively. Uncorrected band gaps are shown in the parentheses. Experimental lattice parameters and band gaps are collected from Refs. [62–68]. Lattice constant ratios are also given with respect to that of GaP.

| | Experimental | | Theoretical | | |
|---|---|---|---|---|---|
| | $a$ (Å) | $E_g$ (eV) | $a$ (Å) | Ratio (%) | $E_g$ (eV) |
| GaP | 5.451[a] | 2.26[g] | 5.456 | | 2.23 (2.26) |
| AlP | 5.463[b] | 2.45[g] | 5.471 | 100.2 | 2.26 (2.28) |
| GaAs | 5.654[c] | 1.52[g] | 5.672 | 103.9 | 1.21 (1.33) |
| AlAs | 5.661[d] | 2.16[g] | 5.676 | 104.0 | 1.99 (2.10) |
| InP | 5.869[e] | 1.42[g] | 5.899 | 108.1 | 1.38 (1.38) |
| InAs | 6.058[f] | 0.42[g] | 6.102 | 111.8 | 0.25 (0.37) |

[a]Reference [62].
[b]Reference [63].
[c]Reference [64].
[d]Reference [65].
[e]Reference [66].
[f]Reference [67].
[g]Reference [68] and references therein.

this work, where interfacial bonds are formed normal to the (111) interfaces as illustrated in Fig. 2(f).

The interface calculations were carried out using a similar setup to the surface calculations using a vacuum layer. Each supercell consisted of either 9 ZB (111) bilayers of phase $A$ and another 9 (111) bilayers of phase $B$, or 9 (100) bilayers of $A$ and another 9 (100) bilayers of $B$. The outer surfaces were separated by a vacuum region of 30 Å, which formed a slab of 18 bilayers with either surface passivated as shown in Figs. 2(c) and 2(f). Both phases $A$ and $B$ were biaxially strained to ILP $= X$. The ps-H atoms and the passivated outermost layer were fixed. The difference in the reference levels $\Delta\varepsilon^{A-B}_{\mathrm{Ref},X}$ was obtained across the interface of interest with respect to the stabilized electrostatic potential of each phase. In all these interface and surface calculations, the supercell dimensions were unchanged.

The atomic structures were visualized by the VESTA package [70]. The electronic structures, i.e., the density of states (DOS) and the electrostatic potentials, were visualized using the PYMATGEN package [71].

## III. RESULTS AND DISCUSSION

### A. Electronic structures of the passivated slabs

As mentioned in the Introduction, a successful passivation fully eliminates the charge transfer from one surface to the other across the slab and stabilizes the electrostatic potential in the bulklike region of the slab. It is seen in Fig. 3 for the GaAs (111) surfaces that the macroscopic averages of the electrostatic potentials converge to nearly constant in both the slab and vacuum regions. The difference between the vacuum level and the reference level $\Delta\varepsilon_{\mathrm{Vac-Ref}}$ is therefore precisely defined for both cation-t and anion-t surfaces. Clearly, $\Delta\varepsilon^{\mathrm{GaAs^{cat}}\ (111)}_{\mathrm{Vac-Ref,GaAs}} = 8.04$ eV and $\Delta\varepsilon^{\mathrm{GaAs^{an}}\ (111)}_{\mathrm{Vac-Ref,GaAs}} = 9.75$ eV include the effects of different surface states and local dipoles with respect to a specific termination. Another significant feature of ps-H passivation is that these ps-H atoms contribute to very localized states that are deep in the valence band and only affect the passivated surface.

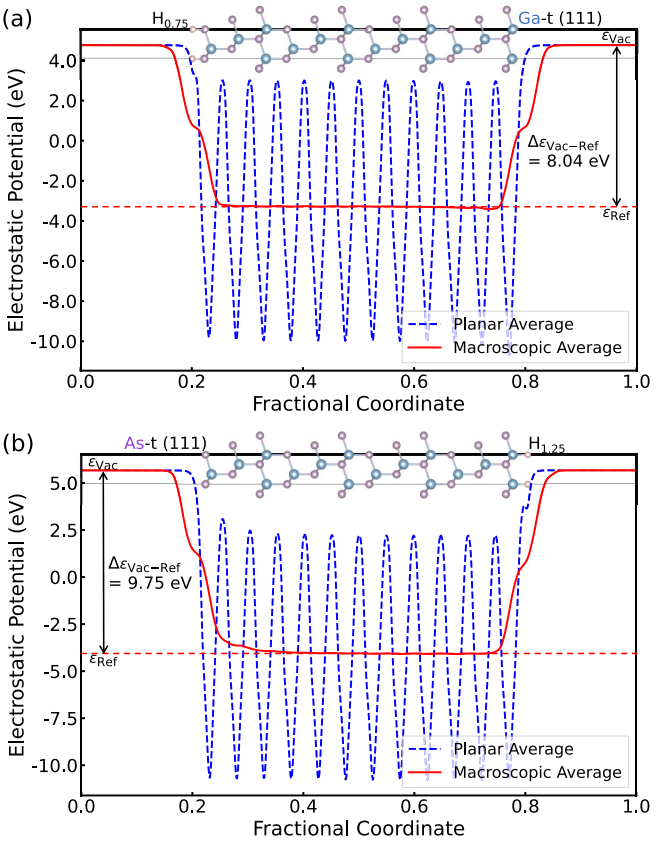


FIG. 3. Electrostatic potentials plotted along the [111] direction of GaAs (111) surface models. The As-t surface in (a) is passivated with $H_{0.75}$ atoms so that reference and vacuum levels are obtained, whereas the Ga-t surface is passivated using $H_{1.25}$ atoms in (b). Corresponding atomic positions in the supercells that contain the (111) bilayers and vacuum regions are also provided.

The electronic structures show that the surface states due to unsaturated bonds are developed from the surface and decay across 4–5 bilayers, whereas no deeper resonances are observed (see Fig. S2 for details [49]). Therefore, considering the alignment of electrostatic potentials used in this study, a stabilized electrostatic potential across at least 3 bilayers around the bulklike region of a slab is necessary to obtain the macroscopic average, and a slab thickness of more than 8 (5+3) bilayers is needed for the proposed passivation scheme. This agrees well with our choice of slab thickness introduced in Sec. II C.

In Fig. 4(b) the nonpolar (110) surface is passivated by both $H_{0.75}$ and $H_{1.25}$ atoms following the EC rule. The 12 (110) layers used contain the same number of atoms as the 12 (111) or (100) bilayers described in Sec. II C. All atoms except for the 3 bilayers adjacent to the passivated surfaces are relaxed, whereas other constraints to the supercell still

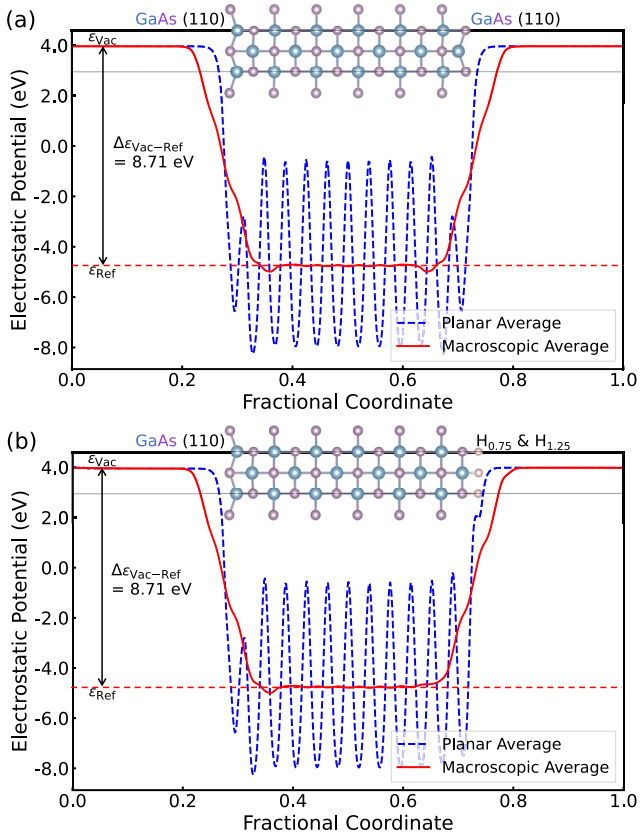


FIG. 4. Electrostatic potentials along the [110] direction of nonpolar GaAs (110) surface models. (a) presents the nonpassivated slab with both (110) surfaces relaxed, whereas dangling bonds on one surface are passivated following the EC rule in (b).

apply. By comparing with the nonpassivated setup shown in Fig. 4(a), it is seen that the passivation mechanism does not essentially impact the obtained reference and vacuum levels.

### B. Ps-H bond length and dipole correction

As the ps-H passivation mechanism is only responsible for eliminating the macroscopic electric field across the slabs, an artificial residual electric field may remain in the vacuum region of the supercell without dipole correction [46] (see Fig. S3 for details [49]). This is due to an artificial charge distribution of the ps-H atoms on the passivated surface and its long-range Coulombic interaction with the electronic states on the other surface across the vacuum, which is also known as the long-range interaction between the surface dipoles. Thus, this residual field features a strong dependence on the length of the ps-H bonds that passivate the surface and can be well or at least partially quenched when a proper bond length is chosen (see Table S1 for details [49]). However, the ps-H bond length has little impact on the calculated $\Delta\varepsilon^{\mathrm{GaAs^{an}}\ (111)}_{\mathrm{Vac-Ref,GaAs}}$ if a proper dipole correction is applied (see Fig. S4 for details [49]). The dipole correction makes optimizing the ps-H bond length an optional procedure, although the passivating ps-H atoms in this work, if possible, still adopt their optimized bond lengths that quench the artificial residual electric fields. The dipole correction thus eliminates very weak residual fields in some cases, e.g., the negligible difference between Figs. 3(b) and S5 [49]. All supercells have been dipole corrected in this work unless additionally specified.

The ps-H bond-length dependence also provides indirect evidence for the effect of the local dipole at the passivated surface. The ps-H surface dipoles depend on not only the charge transfer from/to the ps-H atoms but also their distances from the passivated surface, whereas the ps-H atoms with the desired valence charge following the EC rule are sufficient for eliminating the macroscopic electric field in the slab region, as indicated in Sec. II A. The varying artificial field reflects the change in surface dipole so that a similar effect to the dipole correction is achieved when the net dipole of the ps-H surface region is tuned by optimizing the ps-H bond length.

### C. Interface calculations with ps-H passivation and natural band offsets

As discussed in Sec. II C, the transferable computational setup to interfaces uses the ps-H/$A$/$B$ stack so that the points concluded in earlier sections still apply, i.e., the inhibition of charge transfer from one surface to the other, the elimination of the macroscopic electric field, and the stabilization of the vacuum level with respect to the ps-H bond length or the dipole correction. Thus, the supercell that contains the ps-H/$A$/$B$ stack and a vacuum region enables calculations with a particular focus on the $A^{\mathrm{cat}}/B^{\mathrm{an}}$ or $A^{\mathrm{an}}/B^{\mathrm{cat}}$ interface.

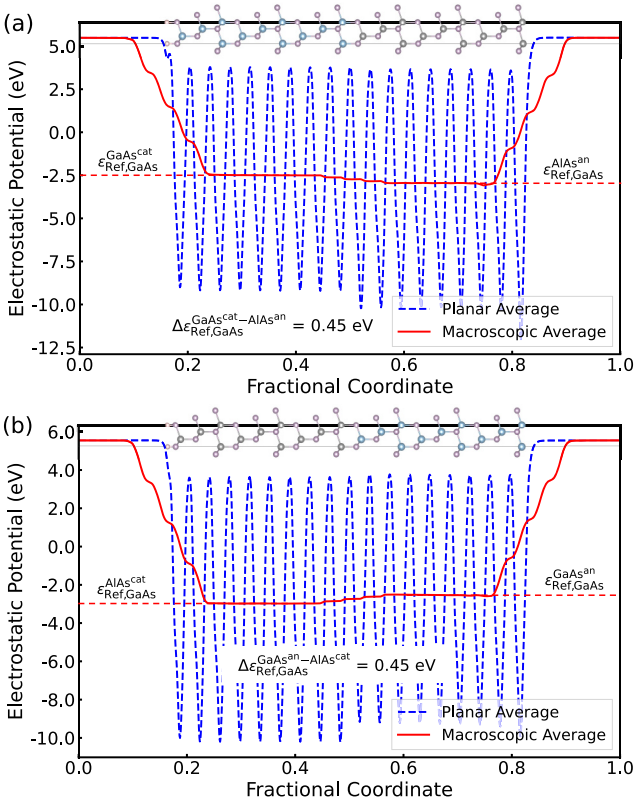


FIG. 5. Electrostatic potentials plotted normal to the GaAs/AlAs (111) interfaces. (a) and (b) represent the $A^{\mathrm{cat}}/B^{\mathrm{an}}$ and $A^{\mathrm{an}}/B^{\mathrm{cat}}$ contacts, respectively, where GaAs is defined as phase $A$ and AlAs as phase $B$. Ga atoms are in blue, As atoms in purple, and Al in gray. The passivation is applied to the As-t surfaces and pink spheres are the ps-H atoms.

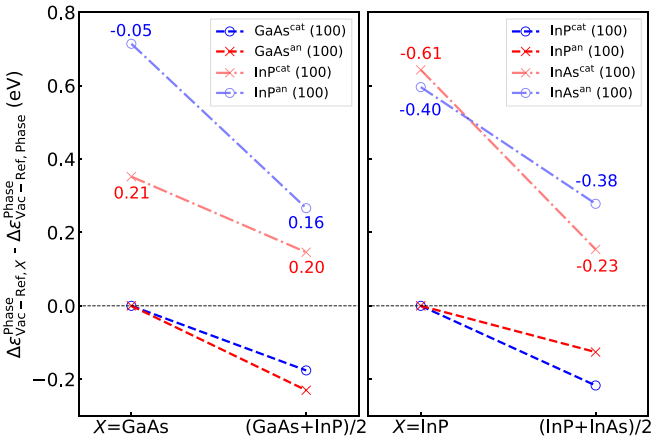


FIG. 6. Effect of varied ILPs determined by comparing $\Delta\varepsilon^{\text{Phase}}_{\text{Vac}-\text{Ref},X}$ in the chosen ILP $= X$ with $\Delta\varepsilon^{\text{Phase}}_{\text{Vac}-\text{Ref},\text{Phase}}$ in its natural ILP. The left panel represents the GaAs/InP (100) interfaces, and the right panel represents the InP/InAs (100) interfaces. In each panel, a pair of dashed (or dash-dotted) lines stand for opposite surface terminations. Moreover, for a given ILP $= X$, two phases in the same color in each panel form an interface of interest. Calculated band offset values without the SOC effect are provided in their corresponding colors.

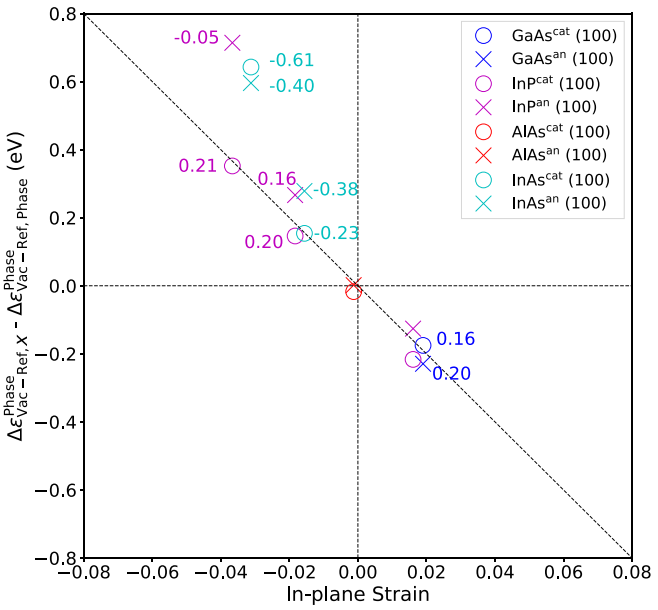


FIG. 7. Effect of varied ILPs determined by comparing $\Delta\varepsilon^{\text{Phase}}_{\text{Vac}-\text{Ref},X}$ in the chosen ILP $= X$ with $\Delta\varepsilon^{\text{Phase}}_{\text{Vac}-\text{Ref},\text{Phase}}$ in its natural ILP, which is plotted against the corresponding in-plane strain of ILP $= X$. Calculated band offsets without the SOC effect are provided in their corresponding colors. Offsets in blue and purple are for the GaAs/InP (100) interfaces; offsets in cyan are for the InP/InAs (100) interfaces.

From the example of $A =$ GaAs and $B =$ AlAs (0.1% in-plane lattice mismatch) shown in Fig. 5, stabilized electrostatic potential profiles are observed in the bulklike regions of $A$ and $B$, together with the vacuum regions. The difference between the reference levels of the two phases is then obtained and shows little dependence on the choice of the $A^{\text{cat}}/B^{\text{an}}$ or $A^{\text{an}}/B^{\text{cat}}$ contact in the case of the GaAs/AlAs (111) interface. The calculated $\Delta\varepsilon^{\text{GaAs}-\text{AlAs}}_{\text{Ref},\text{GaAs}}$ has a negligible deviation of 0.004 eV between the opposite contacts, which is comparable to a common numerical error in this study when taking the macroscopic average.

Nevertheless, when the lattice mismatch is large, its impact increases so that size-induced errors arise by simply using $X = A$. The GaAs/AlP (111) interface serves as a reasonable explanation for this. The (111) ILP of AlP is increased by 3.7% when calculating $\Delta\varepsilon^{\text{AlP}^{\text{cat}}\ (111)}_{\text{Vac}-\text{Ref},\text{GaAs}}$ so that the thickness of the slab along its [111] direction drops accordingly, which results in major rumpling reconstruction of the Al-t (111) surface and, consequently, a shift of the surface states near the band edges to deep states in the band gap. These changes in electronic structure affect the surface band positions with respect to the vacuum level. This brings about an error of $\sim$0.6 eV to the GaAs$^{\text{an}}$/AlP$^{\text{cat}}$ (111) band offset. Since the objective of computing $\Delta\varepsilon^{\text{AlP}^{\text{cat}}\ (111)}_{\text{Vac}-\text{Ref},X} - \Delta\varepsilon^{\text{AlP}^{\text{cat}}\ (111)}_{\text{Vac}-\text{Ref},\text{AlP}}$ is to

TABLE II. Natural valence-band offsets calculated for the heterointerfaces of interest. Offsets are defined as $A-B$ so that a positive offset indicates a higher VBM of $A$ than that of $B$. Corresponding experimental offsets of the same orientations are provided if available. Following the definition in Sec. II C, $A^{\text{cat}}/B^{\text{an}}$ and $A^{\text{an}}/B^{\text{cat}}$ denote two opposite interfaces. Calculated offsets are corrected according to the SOC effect [18], which increases the VBMs by 0.02, 0.03, 0.00, 0.11, 0.12, and 0.12 eV for AlP, GaP, InP, AlAs, GaAs, and InAs, respectively. Uncorrected offsets are shown in the parentheses.

| | | | Calculated $\Delta\varepsilon^{A-B,\text{nat}}_{\text{VBM}}$ (eV) | | |
|---|---|---|---|---|---|
| Interface $A/B$ | Mismatch (%) | ILP $= X$ | $A^{\text{cat}}/B^{\text{an}}$ | $A^{\text{an}}/B^{\text{cat}}$ | Experimental offsets (eV) |
| GaP/AlP (111) | −0.2 | $A$ | 0.57 (0.56) | 0.58 (0.57) | |
| GaP/AlP (100) | −0.2 | $A$ | 0.58 (0.57) | 0.60 (0.59) | 0.57[a] |
| GaAs/AlAs (111) | −0.1 | $A$ | 0.49 (0.48) | 0.56 (0.55) | |
| GaAs/AlAs (100) | −0.1 | $A$ | 0.54 (0.53) | 0.56 (0.55) | 0.55, 0.45[b] |
| GaAs/AlP (111) | 3.7 | $(A+B)/2$ | 1.16 (1.06) | 1.09 (0.99) | |
| GaAs/InP (100) | −4.0 | $(A+B)/2$ | 0.28 (0.16) | 0.32 (0.20) | 0.19[c] |
| InP/InAs (100) | −3.4 | $(A+B)/2$ | −0.50 (−0.38) | −0.35 (−0.23) | −0.31[d] |

[a]Experimental VBM offset for the GaP/AlP/GaP (100) stack from Ref. [72].
[b]Experimental VBM offset for AlAs on GaAs (100) from Refs. [73,74].
[c]Experimental VBM offset for GaAs/InP (100) from Ref. [75].
[d]Experimental VBM offset for InP/InAs (100) from Ref. [75].

include the effects of the IP and EA changes with respect to the ILP, a significant surface reconstruction is undesirable. Therefore, a considerable change in ILP should be avoided in such calculations so that $X = (A + B)/2$ becomes more applicable to interfaces with a large mismatch.

As the effect of a significant ILP change is not necessarily as obvious as that in the GaAs/AlP (111) case with the significant rumpling at the Al-t (111) surface, more quantitative evidence can be found by investigating the GaAs/InP (100) and InP/InAs (100) interfaces. In each case, the effect of the varied ILPs is included by using the expression $\Delta\varepsilon^{\mathrm{Phase}}_{\mathrm{Vac-Ref},X} - \Delta\varepsilon^{\mathrm{Phase}}_{\mathrm{Vac-Ref,Phase}}$, in which Phase $= A$ or $B$, and is compared between $X = A$ and $X = (A + B)/2$ in Fig. 6. Both terminations of a given phase are represented by a pair of dashed or dash-dotted lines in each panel of Fig. 6, whereas the constituent surfaces of an interface are indicated by the same color with respect to a certain ILP $= X$. For example, the $\mathrm{GaAs}^{\mathrm{cat}}/\mathrm{InP}^{\mathrm{an}}$ (100) interface is indicated by the blue circles in the left panel of Fig. 6, and the obtained band offset significantly depends on the difference between these two circles of the same ILP $= X$. Thus, the impact of a significant change in ILP results in possible errors of $\sim$0.3 eV and should be avoided. The mechanism behind this can be roughly elucidated using Fig. 7, in which a linear relationship between $\Delta\varepsilon^{\mathrm{Phase}}_{\mathrm{Vac-Ref},X} - \Delta\varepsilon^{\mathrm{Phase}}_{\mathrm{Vac-Ref,Phase}}$ and the corresponding in-plane strain of ILP $= X$ is found. This linear relationship well applies to in-plane strains smaller than $\pm 2\%$, while some results of larger strains clearly deviate from it. Although such a relationship does not provide a rigorous picture of the impact of the in-plane strain, it can be observed that offset values deviating from this linear relationship are likely to include relatively large errors. Thus, a surface unnecessarily strained biaxially adds to the complexity of the IP or EA analysis and is not desired for the natural band offset.

The VBM offsets for various interfaces are summarized in Table II and compared with their corresponding experimental results. These VBM offsets are also plotted with their corresponding CBM offsets in Fig. 8. In particular, the band offsets obtained using $X = (A + B)/2$ are shown for the GaAs/AlP (111), GaAs/InP (100), and InP/InAs (100) interfaces. In general, the experimental offsets are available for the (100) interfaces, which are very well reproduced by the band offset calculations proposed in this work.

Note that when the two constituent phases share a common cation or anion and extend semi-infinitely normal to the interfaces, the $A^{\mathrm{cat}}/B^{\mathrm{an}}$ and $A^{\mathrm{an}}/B^{\mathrm{cat}}$ (100) interfaces ideally represent the same interface, which applies to GaP/AlP, GaAs/AlAs, and InP/InAs in Table II. Thus, band offsets independent of the $A^{\mathrm{cat}}/B^{\mathrm{an}}$ and $A^{\mathrm{an}}/B^{\mathrm{cat}}$ terminations are expected. In practical calculations using the slab models, such (100) interfaces have the same interfacial composition relative to the ion in common, but the $A^{\mathrm{cat}}/B^{\mathrm{an}}$ and $A^{\mathrm{an}}/B^{\mathrm{cat}}$ models include different surface and interfacial dipole contributions due to the opposite slab terminations. Thus, the proposed method in this article practically treats the $A^{\mathrm{cat}}/B^{\mathrm{an}}$ and $A^{\mathrm{an}}/B^{\mathrm{cat}}$ terminations as different interfaces. However, as the calculated VBM offsets show little dependence on the interfacial configuration of $A^{\mathrm{cat}}/B^{\mathrm{an}}$ or $A^{\mathrm{an}}/B^{\mathrm{cat}}$ in Table II, which agrees well with the discussed ideal interface, it can be concluded

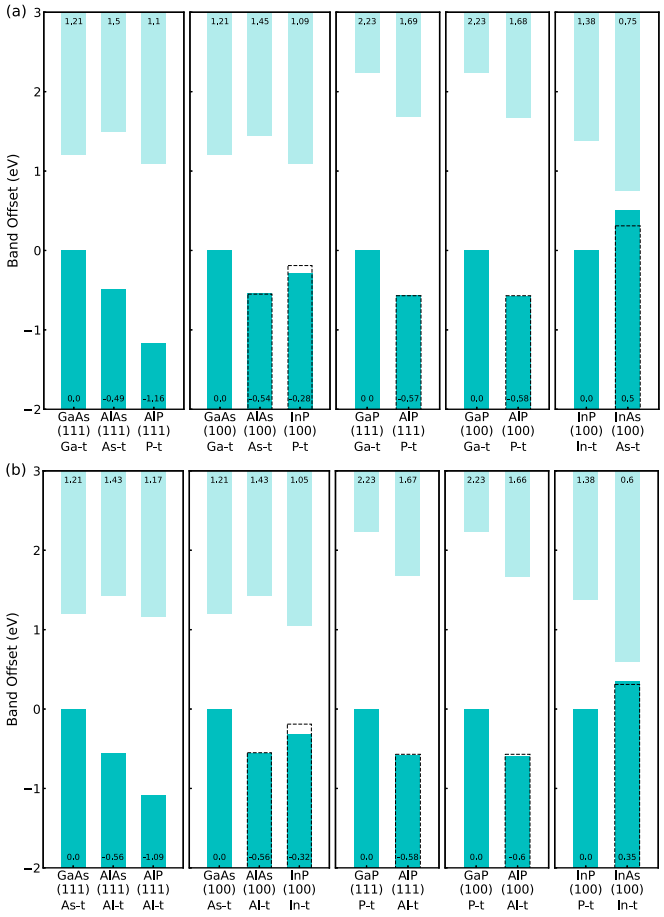


FIG. 8. Natural VBM and CBM offsets for various (111) and (100) interfaces. The upper edges of bars in dark cyan are aligned VBMs and the lower edges of the lighter ones are aligned CBMs. In each subplot, offsets are obtained with respect to the reference phases, whose VBMs are set to zero. These references are GaAs (111), GaAs (100), GaP (111), GaP (100), and InP (100), respectively. Subplots in (a) are for the $A^{\mathrm{cat}}/B^{\mathrm{an}}$ interfaces, whereas the $A^{\mathrm{an}}/B^{\mathrm{cat}}$ interfaces are given in (b). Relative VBM and CBM values are provided in corresponding bars. Relative VBMs obtained experimentally [72–75] are plotted as empty bars outlined by dashed lines in black.

that the surface and interfacial dipole contributions are reasonably treated in both models.

The $A^{\mathrm{cat}}/B^{\mathrm{an}}$ and $A^{\mathrm{an}}/B^{\mathrm{cat}}$ (111) interfaces of a common cation or anion are geometrically different by nature. However, since the interplanar electronic dipole compensation between the (111) planes is equivalent to that between the (100) planes in the ideal ZB crystals, the VBM offsets for such $A^{\mathrm{cat}}/B^{\mathrm{an}}$ and $A^{\mathrm{an}}/B^{\mathrm{cat}}$ configurations are also close to each other regardless of the geometrical difference.

On the contrary, the $A^{\mathrm{cat}}/B^{\mathrm{an}}$ and $A^{\mathrm{an}}/B^{\mathrm{cat}}$ configurations are different in the local chemical composition at the GaAs/InP (100) and GaAs/AlP (111) interfaces. The VBM offsets yet show little interfacial configuration dependence. This is due to the similarities in atomic structure and interfacial chemistry (valence) that contribute to a highly coherent heterojunction. Such coherency is particularly reflected in the interfacial electronic structure, in which the surface electronic states observed for the investigated polar surfaces

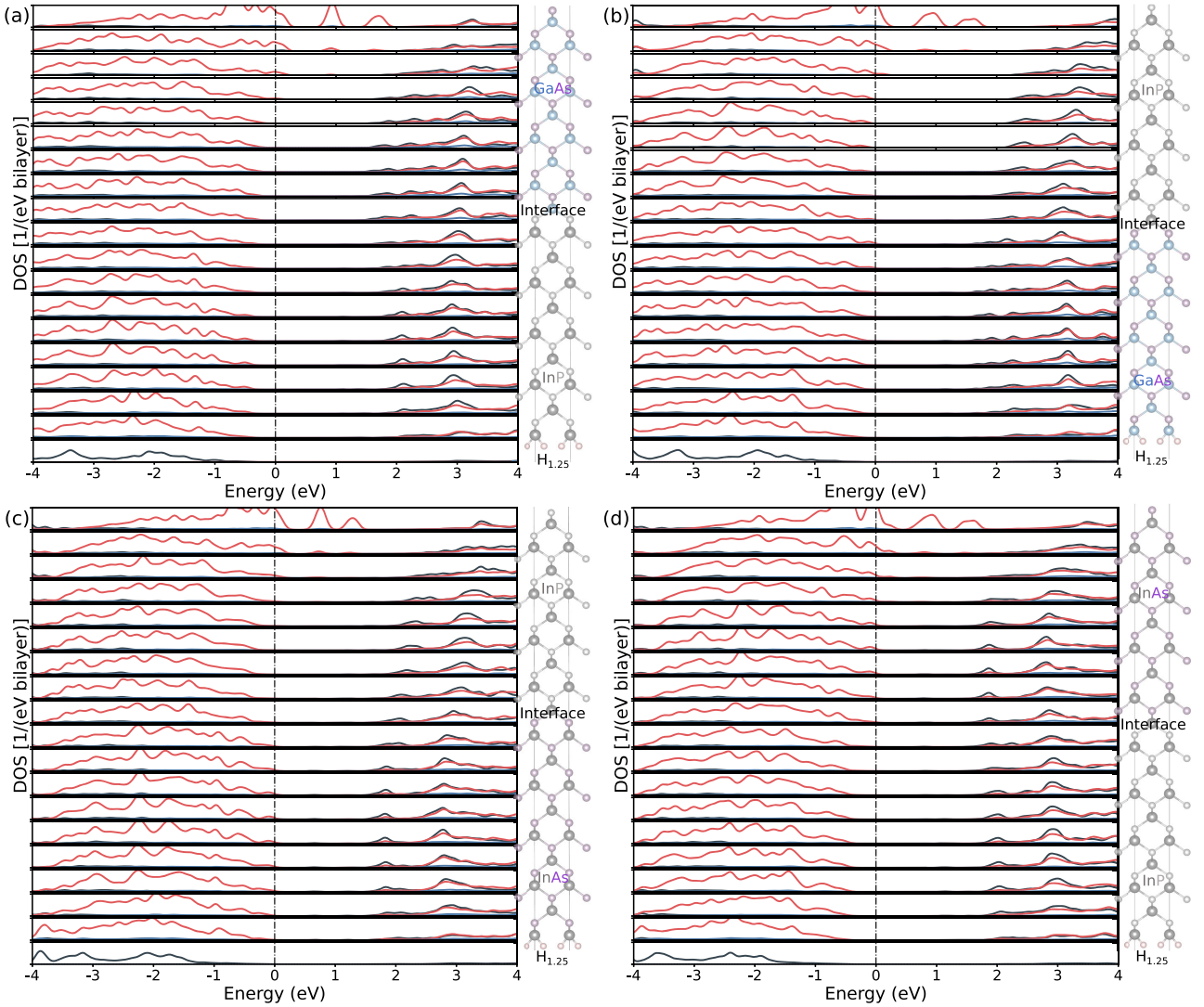


FIG. 9. Layer-resolved DOS plots of the ps-H/*A*/*B* (100) interface slabs with ILPs of $X = (A + B)/2$: (a) $GaAs^{cat}/InP^{an}$, (b) $GaAs^{an}/InP^{cat}$, (c) $InP^{cat}/InAs^{an}$, and (d) $InP^{an}/InAs^{cat}$ interfaces. Each subplot contains the DOS of a (100) bilayer (or a ps-H layer), where the vertical axis covers 0 to 1/(eV bilayer) or 1/(eV ps-H layer). Black, red, and blue curves represent *s*, *p*, and *d* states, respectively. Each energy zero is set to the corresponding Fermi level.

well compensate each other when an interface is formed. It can be seen in Fig. 9 that the ps-H/*A*/*B* interface models exhibit comparable surface states to the corresponding surface models of phase *B*, but such states disappear near the interface regions. This behavior can be attributed to the formation of interfacial chemical bonding that obeys the EC rule. It should be emphasized here that whether such nearly complete interfacial chemical bonding is formed or not significantly depends on the constituent phases of an interface. Investigating less-coherent interfaces with more complex interfacial chemistry and the effect of uncompensated interfacial electronic states together with their associated interfacial dipole contribution should constitute an interesting topic for future study.

## IV. CONCLUSIONS

A strategy to tackle the derivation of the band alignment between polar surfaces and the band offset at a polar interface has been discussed in this work. The proposed method uses ps-H passivation to quench the macroscopic electric field that usually hinders the adoption of commonly used computational setups for band offset calculations. The ps-H passivation mimics a semi-infinite bulk system and prevents the charge transfer due to the presence of dangling bonds on polar surfaces. The passivation stabilizes the electrostatic potential profiles normal to the polar surfaces or interfaces and makes first-principles modeling applicable to the evaluation of band offsets at polar interfaces taking into consideration the interfacial dipole contributions.

The effects of ps-H passivation have been evaluated in significant detail. They are localized on the passivated surface and have a nearly negligible impact on the reference level of the target surface and the vacuum level. The stabilization of the vacuum electrostatic potential is controlled differently from that in the bulklike region, as the latter depends on

the choice of ps-H atoms with a proper number of valence electrons, whereas the former needs to be enhanced by varying the ps-H bond length or by dipole correction. Several prototypical interfaces made of the (100) or (111) surfaces of group III-V ZB semiconductors have been considered in this paper. The proposed method generally well reproduces the VBM offsets experimentally obtained. However, the ILP of the interface model should be carefully chosen when $A$ and $B$ feature a large lattice mismatch, to avoid an undesirably large in-plane strain that impacts the surface results used to estimate the ILP relaxation effect. The calculated interfacial band offsets in this study show little dependence on the $A^{\mathrm{cat}}/B^{\mathrm{an}}$ or $A^{\mathrm{an}}/B^{\mathrm{cat}}$ interfacial configuration, each with an opposite polar slab termination to the other, which is attributed to the well-compensated electronic states across the formed interfaces. As such compensation does not apply to all interfaces, particularly for those composed of structurally and chemically dissimilar materials and those with polarization mismatches induced by spontaneous polarization, the impact of the remaining interfacial states strongly depends on the system of interest and should be investigated separately in the future.

## ACKNOWLEDGMENTS

This work was supported by JST CREST Grant No. JPMJCR17J2 and JSPS KAKENHI Grant No. JP20H00302. The calculations were performed using the TSUBAME3.0 supercomputer at Tokyo Institute of Technology.

[1] J. Robertson, Band offsets of wide-band-gap oxides and implications for future electronic devices, J. Vac. Sci. Technol. B **18**, 1785 (2000).
[2] E. T. Yu, J. O. McCaldin, and T. C. McGill, Band offsets in semiconductor heterojunctions, Solid State Phys. **46**, 1 (1992).
[3] A. Franciosi and C. G. Van de Walle, Heterojunction band offset engineering, Surf. Sci. Rep. **25**, 1 (1996).
[4] J. Robertson, Band offsets, Schottky barrier heights, and their effects on electronic devices, J. Vac. Sci. Technol., A **31**, 050821 (2013).
[5] P. W. Peacock and J. Robertson, Band offsets and Schottky barrier heights of high dielectric constant oxides, J. Appl. Phys. **92**, 4712 (2002).
[6] D. Cahen and A. Kahn, Electron energetics at surfaces and interfaces: Concepts and experiments, Adv. Mater. **15**, 271 (2003).
[7] Y. Ping, D. Rocca, and G. Galli, Electronic excitations in light absorbers for photoelectrochemical energy conversion: First principles calculations based on many body perturbation theory, Chem. Soc. Rev. **42**, 2437 (2013).
[8] Y. Hinuma, A. Grüneis, G. Kresse, and F. Oba, Band alignment of semiconductors from density-functional theory and many-body perturbation theory, Phys. Rev. B **90**, 155405 (2014).
[9] Y. Hinuma, F. Oba, Y. Nose, and I. Tanaka, First-principles study of valence band offsets at $ZnSnP_2$/CdS, $ZnSnP_2$/ZnS, and related chalcopyrite/zincblende heterointerfaces, J. Appl. Phys. **114**, 043718 (2013).
[10] J. Tersoff, Theory of semiconductor heterojunctions: The role of quantum dipoles, Phys. Rev. B **30**, 4874 (1984).
[11] W. Mönch, Empirical tight-binding calculation of the branch-point energy of the continuum of interface-induced gap states, J. Appl. Phys. **80**, 5076 (1996).
[12] A. Schleife, F. Fuchs, C. Rödl, J. Furthmüller, and F. Bechstedt, Branch-point energies and band discontinuities of III-nitrides and III-/II-oxides from quasiparticle band-structure calculations, Appl. Phys. Lett. **94**, 012104 (2009).
[13] L. A. Ledebo and B. K. Ridley, On the position of energy levels related to transition-metal impurities in III-V semiconductors, J. Phys. C: Solid State Phys. **15**, L961 (1982).
[14] M. J. Caldas, A. Fazzio, and A. Zunger, A universal trend in the binding energies of deep impurities in semiconductors, Appl. Phys. Lett. **45**, 671 (1984).
[15] C. G. Van de Walle and J. Neugebauer, Universal alignment of hydrogen levels in semiconductors, insulators and solutions, Nature (London) **423**, 626 (2003).
[16] Y. Li, L. E. O'Leary, N. S. Lewis, and G. Galli, Combined theoretical and experimental study of band-edge control of Si through surface functionalization, J. Phys. Chem. C **117**, 5188 (2013).
[17] V. Stevanović, S. Lany, D. S. Ginley, W. Tumas, and A. Zunger, Assessing capability of semiconductors to split water using ionization potentials and electron affinities only, Phys. Chem. Chem. Phys. **16**, 3706 (2014).
[18] A. Grüneis, G. Kresse, Y. Hinuma, and F. Oba, Ionization Potentials of Solids: The Importance of Vertex Corrections, Phys. Rev. Lett. **112**, 096401 (2014).
[19] H.-J. Sung, Y. Mochizuki, and F. Oba, Surface reconstruction and band alignment of nonmetallic A(II)B(IV)$O_3$ perovskites, Phys. Rev. Mater. **4**, 044606 (2020).
[20] Y. Hinuma, Y. Kumagai, I. Tanaka, and F. Oba, Band alignment of semiconductors and insulators using dielectric-dependent hybrid functionals: Toward high-throughput evaluation, Phys. Rev. B **95**, 075302 (2017).
[21] C. G. Van de Walle and R. M. Martin, Theoretical study of band offsets at semiconductor interfaces, Phys. Rev. B **35**, 8154 (1987).
[22] Y. H. Li, A. Walsh, S. Chen, W. J. Yin, J. H. Yang, J. Li, J. L. F. Da Silva, X. G. Gong, and S. H. Wei, Revised ab initio natural band offsets of all group IV, II-VI, and III-V semiconductors, Appl. Phys. Lett. **94**, 212109 (2009).
[23] Y. Hinuma, F. Oba, Y. Kumagai, and I. Tanaka, Band offsets of $CuInSe_2$/CdS and $CuInSe_2$/ZnS (110) interfaces: A hybrid density functional theory study, Phys. Rev. B **88**, 035305 (2013).
[24] N. Oyama, E. Ohta, K. Takeda, K. Shiraishi, and H. Yamaguchi, First-principles calculation for misfit dislocations in InAs/GaAs(110) heteroepitaxy, Surf. Sci. **433**, 900 (1999).
[25] R. Choudhury, D. R. Bowler, and M. J. Gillan, Atomic structure of misfit dislocations at InAs/GaAs(110), J. Phys.: Condens. Matter **20**, 235227 (2008).
[26] Y. Hinuma, F. Oba, and I. Tanaka, Valence band offsets at zinc-blende heterointerfaces with misfit dislocations: A first-principles study, Phys. Rev. B **88**, 075319 (2013).

[27] J. W. Matthews and A. E. Blakeslee, Defects in epitaxial multilayers: I. Misfit dislocations, J. Cryst. Growth **27**, 118 (1974).
[28] A. Janotti and C. G. Van De Walle, Absolute deformation potentials and band alignment of wurtzite ZnO, MgO, and CdO, Phys. Rev. B **75**, 121201(R) (2007).
[29] E. S. Kadantsev and P. Hawrylak, Absolute deformation potentials and robust ab initio model for band shifts induced by (001) biaxial strain in group IIIA-VA semiconductors, Appl. Phys. Lett. **98**, 023108 (2011).
[30] C. G. Van de Walle and R. M. Martin, Absolute Deformation Potentials: Formulation and Ab Initio Calculations for Semiconductors, Phys. Rev. Lett. **62**, 2028 (1989).
[31] A. Wadehra, J. W. Nicklas, and J. W. Wilkins, Band offsets of semiconductor heterostructures: A hybrid density functional study, Appl. Phys. Lett. **97**, 092119 (2010).
[32] K. Steiner, W. Chen, and A. Pasquarello, Band offsets of lattice-matched semiconductor heterojunctions through hybrid functionals and $G_0W_0$, Phys. Rev. B **89**, 205309 (2014).
[33] P. H. Hünenberger and J. A. McCammon, Ewald artifacts in computer simulations of ionic solvation and ion-ion interaction: A continuum electrostatics study, J. Chem. Phys. **110**, 1856 (1999).
[34] C. Zhang and M. Sprik, Finite field methods for the supercell modeling of charged insulator/electrolyte interfaces, Phys. Rev. B **94**, 245309 (2016).
[35] S. J. Cox and P. L. Geissler, Interfacial ion solvation: Obtaining the thermodynamic limit from molecular simulations, J. Chem. Phys. **148**, 222823 (2018).
[36] T. Sayer and S. J. Cox, Macroscopic surface charges from microscopic simulations, J. Chem. Phys. **153**, 164709 (2020).
[37] A. Wander, F. Schedin, P. Steadman, A. Norris, R. McGrath, T. S. Turner, G. Thornton, and N. M. Harrison, Stability of Polar Oxide Surfaces, Phys. Rev. Lett. **86**, 3811 (2001).
[38] C. Noguera and J. Goniakowski, Polarity in oxide ultrathin films, J. Phys.: Condens. Matter **20**, 264003 (2008).
[39] Y. Hinuma, Y. Kumagai, F. Oba, and I. Tanaka, Categorization of surface polarity from a crystallographic approach, Comput. Mater. Sci. **113**, 221 (2016).
[40] G. Kresse, O. Dulub, and U. Diebold, Competing stabilization mechanism for the polar ZnO(0001)-Zn surface, Phys. Rev. B **68**, 245409 (2003).
[41] D. Mora-Fonz, T. Lazauskas, M. R. Farrow, C. R. A. Catlow, S. M. Woodley, and A. A. Sokol, Why are polar surfaces of ZnO stable? Chem. Mater. **29**, 5306 (2017).
[42] B. E. Gaddy, E. A. Paisley, J.-P. Maria, and D. L. Irving, Overcoming the polarization catastrophe in the rocksalt oxides MgO and CaO, Phys. Rev. B **90**, 125403 (2014).
[43] P. W. Tasker, The stability of ionic crystal surfaces, J. Phys. C: Solid State Phys. **12**, 4977 (1979).
[44] K. Shiraishi, A new slab model approach for electronic structure calculation of polar semiconductor surface, J. Phys. Soc. Jpn. **59**, 3455 (1990).
[45] T. Wang and P. D. Bristowe, A predictive modeling study of the impact of chemical doping on the strength of a Ag/ZnO interface, J. Appl. Phys. **124**, 235304 (2018).
[46] S. H. Yoo, M. Todorova, D. Wickramaratne, L. Weston, C. G. V. de Walle, and J. Neugebauer, Finite-size correction for slab supercell calculations of materials with spontaneous polarization, npj Comput. Mater. **7**, 58 (2021).
[47] N. A. Spaldin, A beginners guide to the modern theory of polarization, J. Solid State Chem. **195**, 2 (2012).
[48] M. D. Pashley, Electron counting model and its application to island structures on molecular-beam epitaxy grown GaAs(001) and ZnSe(001), Phys. Rev. B **40**, 10481 (1989).
[49] See Supplemental Material at http://link.aps.org/supplemental/10.1103/PhysRevMaterials.7.084602 for the figures and table that support the discussion in this paper.
[50] F. Oba and Y. Kumagai, Design and exploration of semiconductors from first principles: A review of recent advances, Appl. Phys. Express **11**, 060101 (2018).
[51] L. Kleinman, Comment on the average potential of a Wigner solid, Phys. Rev. B **24**, 7412 (1981).
[52] P. E. Blöchl, Projector augmented-wave method, Phys. Rev. B **50**, 17953 (1994).
[53] G. Kresse and J. Hafner, Ab initio molecular dynamics for liquid metals, Phys. Rev. B **47**, 558 (1993).
[54] G. Kresse and D. Joubert, From ultrasoft pseudopotentials to the projector augmented-wave method, Phys. Rev. B **59**, 1758 (1999).
[55] G. Kresse and J. Furthmüller, Efficient iterative schemes for ab initio total-energy calculations using a plane-wave basis set, Phys. Rev. B **54**, 11169 (1996).
[56] J. Paier, M. Marsman, K. Hummer, G. Kresse, I. C. Gerber, and J. G. Angyán, Screened hybrid density functionals applied to solids, J. Chem. Phys. **124**, 154709 (2006).
[57] T. L. Gilbert, Hohenberg-Kohn theorem for nonlocal external potentials, Phys. Rev. B **12**, 2111 (1975).
[58] A. Seidl, A. Görling, P. Vogl, J. A. Majewski, and M. Levy, Generalized Kohn-Sham schemes and the band-gap problem, Phys. Rev. B **53**, 3764 (1996).
[59] J. Heyd, G. E. Scuseria, and M. Ernzerhof, Hybrid functionals based on a screened Coulomb potential, J. Chem. Phys. **118**, 8207 (2003).
[60] J. Heyd and G. E. Scuseria, Assessment and validation of a screened Coulomb hybrid density functional, J. Chem. Phys. **120**, 7274 (2004).
[61] A. V. Krukau, O. A. Vydrov, A. F. Izmaylov, and G. E. Scuseria, Influence of the exchange screening parameter on the performance of screened hybrid functionals, J. Chem. Phys. **125**, 224106 (2006).
[62] P. Deus, U. Voland, and H. A. Schneider, Thermal expansion of GaP within 20 to 300 K, Phys. Status Solidi **80**, K29 (1983).
[63] D. Richman, Vapor phase growth and properties of aluminum phosphide, J. Electrochem. Soc. **115**, 945 (1968).
[64] A. S. Cooper, Precise lattice constants of germanium, aluminum, gallium arsenide, uranium, sulphur, quartz and sapphire, Acta Crystallogr. **15**, 578 (1962).
[65] M. Ettenberg and R. J. Paff, Thermal expansion of AlAs, J. Appl. Phys. **41**, 3926 (1970).
[66] A. Addamiano, On the preparation of the phosphides of aluminum, gallium and indium, J. Am. Chem. Soc. **82**, 1537 (1960).
[67] A. G. Thompson, J. E. Rowe, and M. Rubenstein, Preparation and optical properties of $InAs_{1-x}P_x$ alloys, J. Appl. Phys. **40**, 3280 (1969).
[68] W. Mönch, *Semiconductor Surfaces and Interfaces*, 3rd ed. (Springer, Berlin, 2001), Vol. 26.

[69] J. Neugebauer and M. Scheffler, Adsorbate-substrate and adsorbate-adsorbate interactions of Na and K adlayers on Al(111), Phys. Rev. B **46**, 16067 (1992).

[70] K. Momma and F. Izumi, VESTA 3 for three-dimensional visualization of crystal, volumetric and morphology data, J. Appl. Crystallogr. **44**, 1272 (2011).

[71] S. P. Ong, W. D. Richards, A. Jain, G. Hautier, M. Kocher, S. Cholia, D. Gunter, V. L. Chevrier, K. A. Persson, and G. Ceder, Python materials genomics (Pymatgen): A robust, open-source python library for materials analysis, Comput. Mater. Sci. **68**, 314 (2013).

[72] S. Nagao, T. Fujimori, H. Gotoh, H. Fukushima, T. Takano, H. Ito, S. Koshihara, and F. Minami, Type-II photoluminescence from GaP/AlP/GaP quantum wells, J. Appl. Phys. **81**, 1417 (1997).

[73] J. Batey and S. L. Wright, Energy band alignment in GaAs:(Al,Ga) as heterostructures: The dependence on alloy composition, J. Appl. Phys. **59**, 200 (1986).

[74] W. I. Wang and F. Stern, Valence band offset in AlAs/GaAs heterojunctions and the empirical relation for band alignment, J. Vac. Sci. Technol. B **3**, 1280 (1985).

[75] J. R. Waldrop, R. W. Grant, and E. A. Kraut, Measurement of GaAs/InP and InAs/InP heterojunction band offsets by x-ray photoemission spectroscopy, Appl. Phys. Lett. **54**, 1878 (1989).

# Supplemental Material – Slab surface passivation and its application to band offset calculations for polar heterointerfaces of zinc-blende semiconductors

Tianwei Wang* and Fumiyasu Oba*
Laboratory for Materials and Structures, Institute of Innovative Research,
Tokyo Institute of Technology, Yokohama 226-8503, Japan

* Corresponding authors.
E-mail addresses: wang@msl.titech.ac.jp (T. Wang), oba@msl.titech.ac.jp (F. Oba).

This supplemental material contains the figures and table that support the discussion in the article.

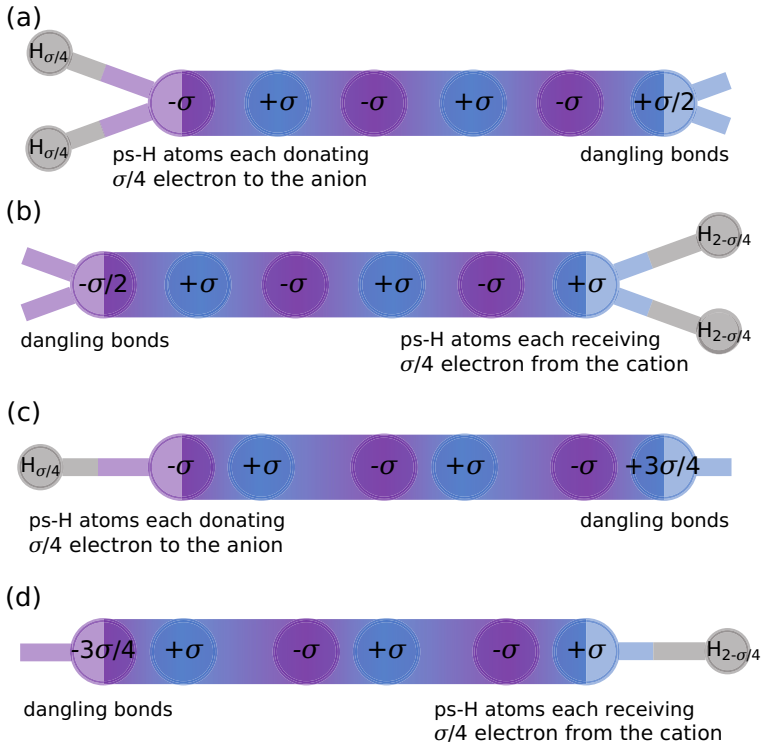


**FIG. S1.** Schematics of the EC rule and the passivation of ZB polar surfaces using ps-H atoms: (a) passivating the (100) anion-t surface, (b) passivating the (100) cation-t surface, (c) passivating the (111) anion-t surface, and (d) passivating the (111) cation-t surface. The saturated bonds are represented by wide rectangles, while the dangling and passivated bonds are narrow rectangles. The circles in gray are ps-H atoms. Each circle represents a plane of corresponding ions/atoms that bi-axially extends parallel with the surface of interest.

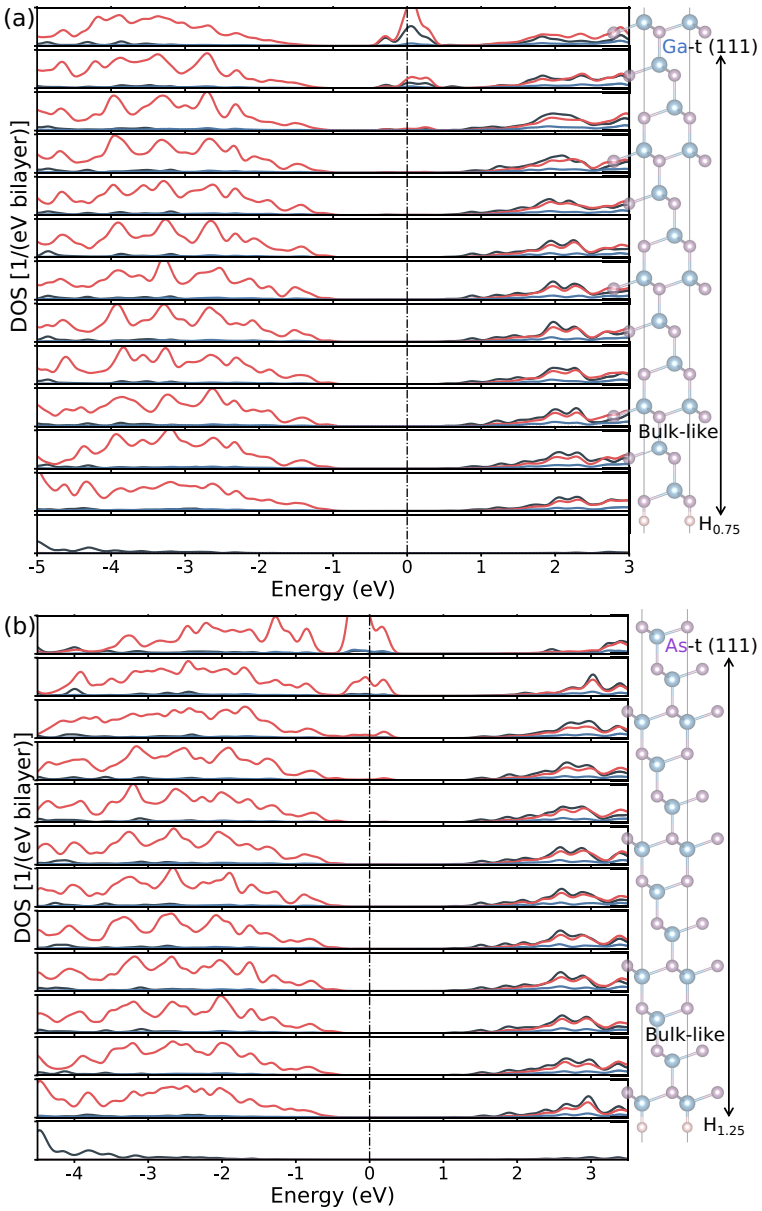


**FIG. S2.** Layer-resolved DOS plots of the ps-H passivated GaAs (111) surface models. Plot (a) is the DOS of the Ga-t surface model, and (b) is that of the As-t surface model. In both plots, each panel includes the DOS of a (111) bilayer (or a ps-H layer), where the vertical axis covers from 0 to 1/(eV bilayer) or 1/(eV ps-H layer). In the bilayer-resolved DOS, the black, red, and blue curves represent the *s*-, *p*-, and *d*-states, respectively. The energy zero is set at the Fermi level.

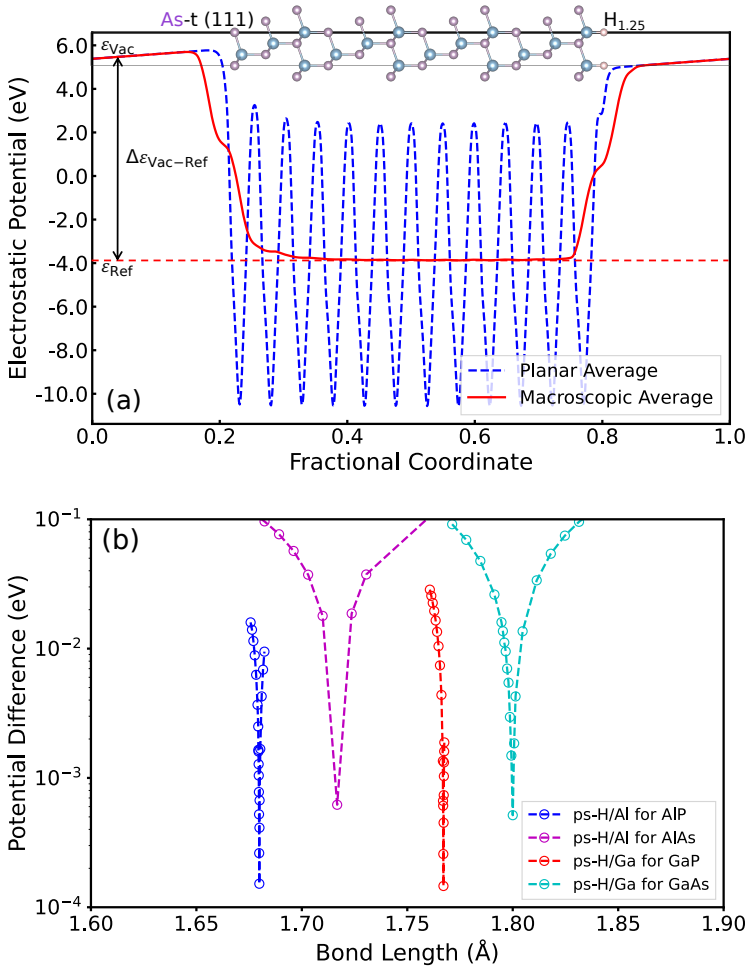


**FIG. S3.** (a) The electrostatic potential along the [111] direction of the GaAs (111) surface model. The convergence is only observed for the slab region while an artificial residual field exits in the vacuum as the dipole correction is turned off. (b) The residual fields for various (111) surfaces quenched by optimizing the ps-H bond length. The residual field is measured as the difference between the maximum and the minimum of the sloped electrostatic potential of the vacuum region.

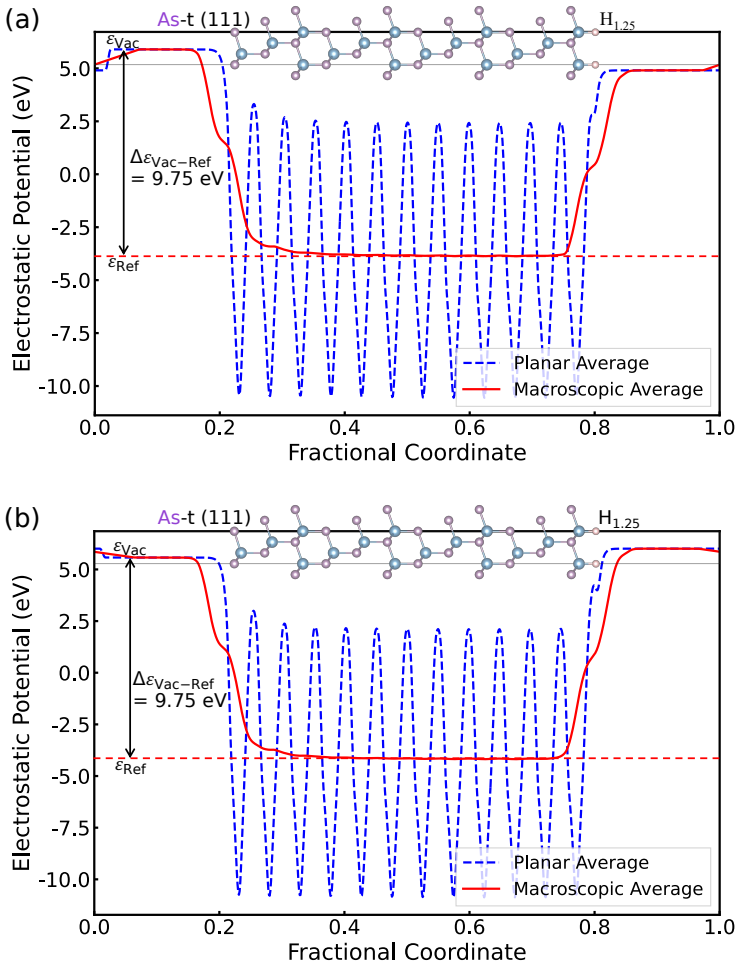


**FIG. S4.** Electrostatic potentials plotted along the [111] direction of the GaAs (111) surface models with the Ga-t surface passivated by $H_{1.25}$. Both include the dipole correction but without using the optimized $H_{1.25}$ bond length. Electrostatic potentials are shown for longer and shorter $H_{1.25}$ bonds than the optimized distance in (a) and (b), respectively.

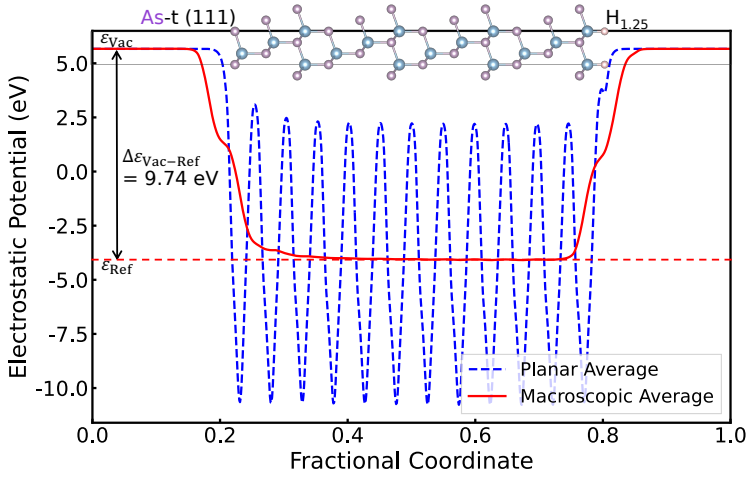


**FIG. S5.** Electrostatic potentials plotted along the [111] direction of the GaAs (111) surface models with the Ga-t surface passivated by $H_{1.25}$. The dipole correction is not included but a very similar result to those in Fig. 3(b) and Fig. S4(b) is obtained since $H_{1.25}$ atoms adopt the optimized bond length.

**TABLE S1.** Optimized ps-H bond lengths for all passivated surfaces in their natural ILPs and their corresponding residual potential differences.

| Passivated surface | Ps-H bonds | Bond length (Å) | Residual (eV) |
|---|---|---|---|
| GaP (111) P-t | P-$H_{0.75}$ | 0.937 | 6.4E-2 |
| GaP (111) Ga-t | Ga-$H_{1.25}$ | 1.767 | 1.5E-4 |
| GaP (100) P-t | P-$H_{0.75}$ | 1.272 | 4.7E-1 |
| GaP (100) Ga-t | Ga-$H_{1.25}$ | 1.591 | 1.1E-2 |
| AlP (111) P-t | P-$H_{0.75}$ | 1.769 | 5.2E-4 |
| AlP (111) Al-t | Al-$H_{1.25}$ | 1.680 | 1.5E-4 |
| AlP (100) P-t | P-$H_{0.75}$ | 1.236 | 5.6E-1 |
| AlP (100) Al-t | Al-$H_{1.25}$ | 1.489 | 7.4E-3 |
| GaAs (111) As-t | As-$H_{0.75}$ | 1.475 | 9.7E-4 |
| GaAs (111) Ga-t | Ga-$H_{1.25}$ | 1.800 | 5.2E-4 |
| GaAs (100) As-t | As-$H_{0.75}$ | 1.423 | 3.9E-1 |
| GaAs (100) Ga-t | Ga-$H_{1.25}$ | 1.601 | 1.9E-3 |
| AlAs (111) As-t | As-$H_{0.75}$ | 1.607 | 3.3E-4 |
| AlAs (111) Al-t | Al-$H_{1.25}$ | 1.717 | 6.2E-4 |
| AlAs (100) As-t | As-$H_{0.75}$ | 1.374 | 4.9E-1 |
| AlAs (100) Al-t | Al-$H_{1.25}$ | 1.514 | 5.8E-3 |
| InP (100) P-t | P-$H_{0.75}$ | 1.373 | 3.2E-2 |
| InP (100) In-t | In-$H_{1.25}$ | 1.691 | 9.3E-5 |
| InAs (100) As-t | As-$H_{0.75}$ | 1.373 | 5.3E-4 |
| InAs (100) In-t | In-$H_{1.25}$ | 1.667 | 6.1E-4 |